Why pacing frequency affects the production of early afterdepolarizations in cardiomyocytes: An explanation revealed by slow-fast analysis of a minimal model

Theodore Vo[1] and Richard Bertram[2,*]

[1]*Department of Mathematics, Florida State University, Tallahassee, Florida 32306, USA*

[2]*Department of Mathematics and Programs in Neuroscience and Molecular Biophysics, Florida State University, Tallahassee, Florida 32306, USA*

(Received 13 March 2019; published 7 May 2019)

Early afterdepolarizations (EADs) are pathological voltage oscillations in cardiomyocytes that have been observed in response to a number of pharmacological agents and disease conditions. Phase-2 EADs consist of small voltage fluctuations during the plateau of an action potential, typically under conditions in which the action potential is elongated. Although a single-cell behavior, EADs can lead to tissue-level arrhythmias. Much is currently known about the biophysical mechanisms (i.e., the roles of ion channels and intracellular Ca^{2+} stores) for the various forms of EADs, due partially to the development and analysis of mathematical models. This includes the application of slow-fast analysis, which takes advantage of timescale separation inherent in the system to simplify its analysis. We take this further, using a minimal three-dimensional model to demonstrate that phase-2 EADs are canards formed in the neighborhood of a folded node singularity. This allows us to predict the number of EADs that can be produced for a given parameter set, and provides guidance on parameter changes that facilitate or inhibit EAD production. With this approach, we demonstrate why periodic stimulation, as occurs in intact heart, preferentially facilitates EAD production when applied at low frequencies. We also explain the origin of complex alternan dynamics that can occur with intermediate-frequency stimulation, in which varying numbers of EADs are produced with each pulse. These revelations fall out naturally from an understanding of folded node singularities, but are difficult to glean from knowledge of the biophysical mechanism for EADs alone. Therefore, understanding the canard mechanism is a useful complement to understanding of the biophysical mechanism that has been developed over years of experimental and computational investigations.

DOI: 10.1103/PhysRevE.99.052205

I. INTRODUCTION

In the normal heart, each heartbeat is associated with an action potential (AP). The cardiac AP consists of a depolarized phase in which the voltage is elevated; this is associated with transient increased permeability of the cell membrane to Na^+ and Ca^{2+}. The depolarized phase is followed by a repolarization to the resting membrane potential, associated with increased permeability to K^+ ions. These changes in the membrane potential lead to a sequence of events that result in contraction of the heart muscle, allowing for pumping of blood through the body.

Early afterdepolarizations (EADs) are pathological voltage oscillations observed in heart muscle cells (cardiomyocytes) during the repolarizing phase of the cardiac AP under conditions in which the AP is elongated (Fig. 1). EADs can be induced by hypokalemia [1,2], as well as oxidative stress [3]. They are also often observed following the administration of drugs that act on K^+, Na^+, or Ca^{2+} ion channels [2,4–11]. These drug-induced EADs can lead to ventricular tachyarrhythmias [5,12,13]. Genetic defects in Na^+ and K^+ channels that prolong the action potential duration can also lead to an increased rate of EADs and risk of sudden death [14].

EADs have been associated with long-QT syndrome [9], and long been recognized as a mechanism for the generation of premature ventricular complexes (PVCs) in the electrocardiogram [15]. Different ventricular arrhythmias, including torsade de pointes, are thought to be initiated by PVCs stemming from EADs [9,16–18]. That is, EADs at the myocyte level have been implicated as the primary mechanism promoting arrhythmias at the tissue level in acquired and congenital long-QT syndromes, including polymorphic ventricular tachycardia and ventricular fibrillation [5,19,20].

In this study, we investigate EADs from an alternative perspective that views the phenomenon as one that can be understood in terms of dynamical systems, complementing the biophysical perspective couched in the language of ionic currents. When viewed as a multitimescale phenomenon that occurs due to twisting and interacting geometric structures that control the flow of the system, it becomes possible to determine conditions facilitating EADs, and maneuvers that can be performed to eliminate them. It also becomes evident why the frequency at which the cell is stimulated is important in determining whether EADs occur, and if so, how many there will be (and thus the duration of the extended AP).

Numerous mathematical models have been constructed at the cellular level to study the genesis of EADs [2,21–24]. These confirmed the importance of increased inward Ca^{2+} current and decreased outward K^+ current in the production of EADs. They also confirmed that reactivation of Ca^{2+} current is a key element of EAD production [1,24]. Modeling at the tissue level has also been done, in this case to understand

*Corresponding author: bertram@math.fsu.edu

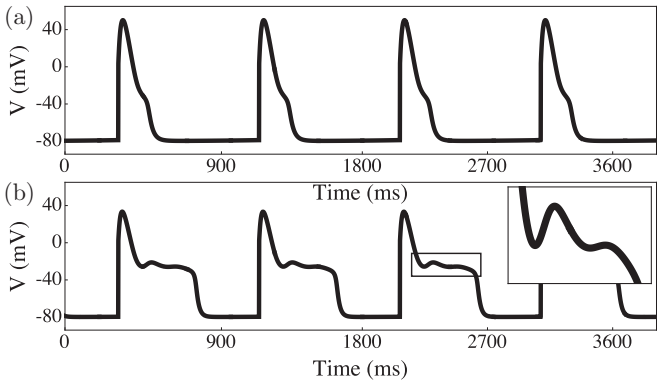

FIG. 1. Representative (a) healthy APs and (b) APs with EADs in a model cardiomyocyte [system (1)]. EADs occur during the repolarizing phase of prolonged APs.

EAD propagation, synchronization, and the genesis of arrthymia [25–28]. These studies demonstrated that EADs at the cellular level can lead to arrhythmias at the tissue level, as has been suggested in experimental studies.

A useful analysis technique for understanding the behavior of models of excitable systems such as cardiomyocytes separates system variables into those that change on a fast timescale and those that change on a slow timescale, and then analyzes the two subsystems and their interaction [29]. This slow-fast analysis has been used to understand the genesis of EADs, using a three-variable model in which two variables were treated as "fast" and one treated as "slow." It was shown that EADs can arise via a delayed subcritical Hopf bifurcation of the fast subsystem [23,30]. This explanation, while providing insights, is limited in its descriptive capabilities. For example, it provides limited information on parameter sets for which EADs may occur, and it does not allow one to predict the number of EADs that are produced when they do occur.

Recently, it was demonstrated that EADs can be attributed to folded-node singularities and their accompanying canard orbits [31]. This was done with the same three-variable model for cardiac APs, but now treating one variable as fast and the other two as slow. Such a splitting provides the potential for insights not available with the 1-slow-2-fast splitting, as demonstrated in [31] and in an earlier publication that focused on electrical bursting in pituitary cells [32]. In particular, the canards of a folded node act as phase and parameter space boundaries, separating orbits with different rotational properties. The folded node singularities are the means by which the existence of these canards can be determined and their properties calculated. Thus, by tracking folded nodes and their associated canards, it is possible to determine regions of parameter space in which EADs occur.

Ventricular cardiomyocytes are, in a physiological setting, subject to periodic stimulation from upstream cardiac cells, originating at the sinoatrial node. Prior experimental and modeling studies have demonstrated that EADs occur more readily at low pacing frequencies than at high frequencies [2,24,33]. At intermediate frequencies the dynamics are complex, consisting of alternans with varying numbers of EADs at each stimulus, a behavior described as "dynamical chaos" [2,23]. The primary goal of this article is to provide an understanding for these phenomena. To achieve this, we use the same minimal cardiac AP model developed in [2] and used recently in [31], and apply a 2-slow-1-fast splitting. We demonstrate that the effects of periodic stimulation of the model cell can be understood precisely using canard theory [34–36]. In particular, we show that the number of EADs produced by a stimulus depends on where it injects the trajectory relative to the canards, and with this knowledge we demonstrate why low-frequency pacing is expected to yield more EADs than is high-frequency pacing. We also demonstrate the origin of the "dynamical chaos" that occurs at intermediate-frequency pacing. Finally, we demonstrate why drugs that inhibit the opening of K^+ channels facilitate EADs, and why EADs can be induced by hypokalemia [1,2,5].

II. MODEL

We study a low-dimensional model for the electrical activity in a cardiomyocyte [2]

$$\begin{aligned} C_m\frac{dV}{dt} &= -(I_{\rm K}+I_{\rm Ca})+I_{\rm sti},\\ \frac{dn}{dt} &= \frac{n_\infty(V)-n}{\tau_n},\\ \frac{dh}{dt} &= \frac{h_\infty(V)-h}{\tau_h}, \end{aligned} \tag{1}$$

where $I_{\rm K}$ is a repolarizing K^+ current, $I_{\rm Ca}$ is a depolarizing Ca^{2+} current, and $I_{\rm sti}$ is a pacemaking stimulus current. System (1) excludes the depolarizing Na^+ current since it is inactivated during the plateau of the AP and has almost no effect on EADs [37]. Here, V is the membrane potential across the cell, n the activation variable for the K^+ channels, and h the inactivation variable for the L-type Ca^{2+} channels. The ionic currents are

$$I_{\rm K}=g_K n(V-V_{\rm K}) \text{ and } I_{\rm Ca}=g_{Ca}m_\infty(V)h(V-V_{\rm Ca}),$$

and the stimulus current provides the system with square wave pulses of 1-ms duration and 40-μA/cm^2 amplitude at a frequency set by the pacing cycle length (PCL),

$$I_{\rm sti}=40\sum_{k\in\mathbb{N}}\{H(t-k\cdot{\rm PCL})-H(t-[k\cdot{\rm PCL}+1])\}.$$

(Here $H(\cdot)$ is the Heaviside function.) The steady state activation and inactivation functions are

$$x_\infty(V)=\frac{1}{1+\exp\left(\frac{V_x-V}{s_x}\right)},\quad h_\infty(V)=\frac{1}{1+\exp\left(\frac{V-V_h}{s_h}\right)},$$

where $x\in\{m,n\}$. Unless stated otherwise, the parameters are fixed at the values in Table I (same as in [2]).

The model cell (1) exhibits two distinct AP morphologies: regular APs and APs with EADs. We use the Farey sequence notation 1^s to denote a single large-amplitude AP with s small-amplitude EADs. Thus, a regular AP is denoted 1^0 and an AP with two EADs is denoted 1^2. More complicated rhythms are described using concatenations of these Farey sequences. For instance, a rhythm that periodically exhibits three regular APs followed by a single AP with two EADs is denoted $(1^0)^3(1^2)$.

Time series in this article were generated by integrating (1) using fourth-order Runge-Kutta, as implemented in

TABLE I. Parameters used in the minimal model (1).

Param	Value	Definition
C_m	0.5 μF/cm^2	Membrane capacitance
g_{Ca}	0.025 mS/cm^2	Max conductance Ca^{2+} channels
g_K	0.04 mS/cm^2	Max conductance K^+ channels
V_{Ca}	100 mV	Reversal potential for Ca^{2+}
V_K	−80 mV	Reversal potential for K^+
τ_n	300 ms	K^+ activation time const
τ_h	80 ms	Ca^+ activation time const
V_m	−35 mV	Voltage at midpoint of $m_\infty(V)$
s_m	6.24 mV	Slope parameter of $m_\infty(V)$
V_n	−40 mV	Voltage at midpoint of $n_\infty(V)$
s_n	5 mV	Slope parameter of $n_\infty(V)$
V_h	−20 mV	Voltage at midpoint of $s_\infty(V)$
s_h	8.6 mV	Slope parameter of $s_\infty(V)$

XPP [38]. Bifurcation diagrams were computed using the numerical continuation software AUTO-07P [39]. The attracting and repelling slow manifolds, and canard solutions, were also computed in AUTO-07P by solving two-point boundary value problems. We refer to [40,41] for details on how the slow manifold and canard computations can be implemented.

III. RESULTS

We now present the main results of the article. First, we demonstrate the variety of AP morphologies of (1) exhibited under various PCLs, including regular APs, APs with EADs, and EAD alternans. Next, we show that the EADs arise from canard dynamics. A similar demonstration was provided by [31], but we elaborate on how the EADs emerge as the cell capacitance is increased from 0 (i.e., moving the system away from the singular limit), and we demonstrate how the rotational sectors determine the number and duration of EADs. Moreover, we demonstrate how drugs that inhibit K^+ channels or a hypokalemic environment can facilitate EAD production. Finally, we completely explain the variety of AP and EAD morphologies exhibited under various PCLs in terms of canard-induced mixed-mode oscillations.

A. Action potential duration and number of EADs increases with PCL

The model cell (1) is entrained to the periodic stimulus; for the parameter set in Table I, the cell exhibits 1^s impulses with period set by the PCL. For small PCLs (i.e., high-frequency pulsing), the attractor is a 1^2 rhythm [Fig. 2(a)]. For intermediate PCLs (1240 ms $\lesssim$ PCL $\lesssim$ 1435 ms), the cell exhibits complex EAD activity, including $1^2 1^3$ alternans [Fig. 2(b)] and $1^2(1^3)^3$ rhythms [Fig. 2(c)]. For large PCLs (i.e., low-frequency pulsing), the cell is in a 1^3 state [Fig. 2(d)].

We summarize the behavior of the model cell and its response to periodic stimulation at various frequencies in Fig. 2(e). We used a dynamic restitution protocol [42] in which the cell was paced at a fixed PCL until steady state was reached, after which the action potential duration (APD) and PCL were recorded. We took the APD to be the time the cell spends with $V > -70$ mV. With this choice of restitution protocol, the PCL is the sum of the APD and the diastolic interval, so our bifurcation diagram encodes the restitution curves [i.e., the plot of the APD as a function of the diastolic interval has the same qualitative features as shown in Fig. 2(e)].

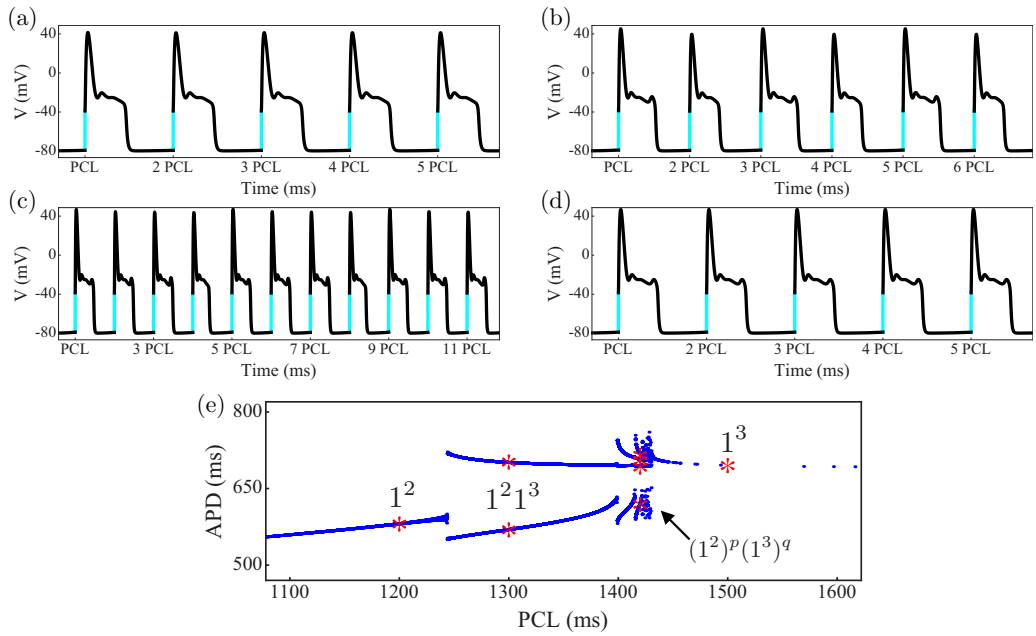

FIG. 2. Dynamics of the model cardiomyocyte (1) under variations in PCL. In (a)–(d), the stimulus pulse is "on" during the cyan segments. The attractor shows (a) 1^2 APs with EADs for PCL = 1200 ms, (b) $1^2 1^3$ alternans for PCL = 1300 ms, (c) $1^2(1^3)^3$ APs with EADs for PCL = 1420 ms, and (d) 1^3 APs with EADs for PCL = 1500 ms. (e) APD versus PCL bifurcation diagram. There is an intermediate band of PCLs (1240 ms $\lesssim$ PCL $\lesssim$ 1435 ms) over which the attractor has complex EAD signature. Red markers indicate the PCLs corresponding to the time series in panels (a)–(d).

The bifurcation diagram shows that periodic stimulation elicits three types of behavior. For high- and low-frequency stimulation, the model cell is in a purely 1^2 or 1^3 state, respectively. In the intermediate-frequency range, the model cell has complex signature of the form $(1^2)^p(1^3)^q$, where p and q are integers. The AP signature becomes more complicated near the transition to the 1^3 state. This increasing complexity of the AP signature near a transition is robust; it occurs for a wide range of g_K and g_{Ca} in (1) and has also been observed in other forced conductance-based cardiomyocyte models [2,23].

B. EADs arise from canard dynamics

We now show that the dynamical mechanisms responsible for EADs are canards. To facilitate the analysis, we consider (1) with no stimulus. We will show that (1) has a slow-fast structure, use this slow-fast splitting to identify the geometric cast of characters involved in EADs, and demonstrate that folded node canards generate EADs, and these canards are robust in parameters. Finally, we explain why inhibition of K^+ channels or a hypokalemic environment facilitates EAD production.

1. The dynamics evolve over multiple timescales

A key observation is that the dynamics evolve over multiple timescales, with slow depolarized or hyperpolarized epochs interspersed by rapid transitions. We show this multitimescale structure by introducing dimensionless variables, v and t_s, via

$$v = \frac{V}{k_V} \quad \text{and} \quad t_s = \frac{t}{k_t},$$

where $k_V = 100$ mV and $k_t = \tau_n = 300$ ms are reference voltage and timescales, respectively. With these rescalings, (1) in the absence of any stimulus becomes

$$\begin{aligned} \varepsilon \frac{dv}{dt_s} &= f(v,n,h), \\ \frac{dn}{dt_s} &= \frac{k_t}{\tau_n}(n_\infty(v) - n) \equiv g_1(v,n), \\ \frac{dh}{dt_s} &= \frac{k_t}{\tau_h}(h_\infty(v) - h) \equiv g_2(v,h), \end{aligned} \tag{2}$$

where

$$f(v,n,h) = -\bar{g}_K n(v - \overline{V}_{\mathrm{K}}) - \bar{g}_{Ca} m_\infty(v) h(v - \overline{V}_{\mathrm{Ca}}),$$

and $\bar{g}_u = \frac{g_u}{g_{\mathrm{ref}}}$ and $\overline{V}_u = \frac{V_u}{k_V}$ for $u \in \{\mathrm{K}, \mathrm{Ca}\}$ denote dimensionless conductances and reversal potentials, respectively. Here, g_{ref} is a reference conductance, and $\varepsilon = \frac{C_m/g_{\mathrm{ref}}}{k_t} \ll 1$ is the ratio of the voltage and reference timescales. The benefit of recasting (1) in dimensionless form (2) is that it reveals the timescales in the model. The voltage is fast (timescale $\frac{C_m}{g_{\mathrm{ref}}} \approx 5$ ms for $C_m = 0.5\,\mu\mathrm{F/cm}^2$ and $g_{\mathrm{ref}} = 0.1\,\mathrm{mS/cm}^2$). The activation variable, n, is slow (timescale $\tau_n = 80$ ms), and the inactivation variable, h, is superslow (timescale $\tau_h = 300$ ms). Thus, (2) is a three-timescale problem.

We stress that the specific values chosen for k_V and k_t do not change the intrinsic slow-fast structure in the system. Moreover, the dimensionless formulation (2) is a necessary formality for the slow-fast analysis. All plots and results from the geometric analysis will be shown in terms of the original dimensional variables.

An effective approach to the analysis of multitimescale problems is Geometric Singular Perturbation Theory (GSPT) [43–45]. The idea is to decompose a slow-fast system into lower dimensional slow and fast subsystems, analyze these subsystems, and combine their information to understand the origin and properties of the dynamics of the original model. The GSPT approach, however, is limited to two-timescale (i.e., slow-fast) problems. In three-timescale systems such as (2), a choice is usually made: group v and n as "fast," or group n and h as "slow."

Prior studies of (1) grouped v and n as fast, and treated h as slow [2]. In this 1-slow-2-fast approach, EADs arise because the depolarized steady state of the (v,n) subsystem loses stability via a Hopf bifurcation leading to oscillations which are destroyed at a homoclinic bifurcation [23,27,46]. While this mechanism is consistent with the *in vitro* and *in silico* observations that EADs appear irregularly under periodic stimulation, it does not provide insight into how many EADs should be observed or why the number of EADs changes with PCL. Here, we treat v as fast, and group n and h as slow. This 2-slow-1-fast approach will allow us to predict the maximal number of EADs that can be generated, and explain why the number of EADs changes with PCL.

2. Underlying geometric structure

We now identify the geometric features that organize the EADs and APs. We begin by reformulating (2) in terms of the fast time, $t_f = \frac{1}{\varepsilon} t_s$, which gives

$$\begin{aligned} \frac{dv}{dt_f} &= f(v,n,h), \\ \frac{dn}{dt_f} &= \varepsilon\, g_1(v,n), \\ \frac{dh}{dt_f} &= \varepsilon\, g_2(v,h). \end{aligned} \tag{3}$$

System (3) is equivalent to (2) in the sense that solutions of both systems trace out the same paths in the (v,n,h) phase space, just at different speeds. We have seen that the dynamics of (1) alternate between slow and fast epochs. The rapid transitions between depolarized and repolarized phases are approximated by solutions of the one-dimensioanl (1D) *fast subsystem*

$$\begin{aligned} \frac{dv}{dt_f} &= f(v,n,h), \\ \frac{dn}{dt_f} &= 0, \\ \frac{dh}{dt_f} &= 0, \end{aligned} \tag{4}$$

obtained by taking the singular limit $\varepsilon \to 0$ in (3). The fast subsystem is the approximation of (2) in which the slow variables move so slowly that they are fixed. Similarly, the slow depolarized or repolarized dynamics are approximated

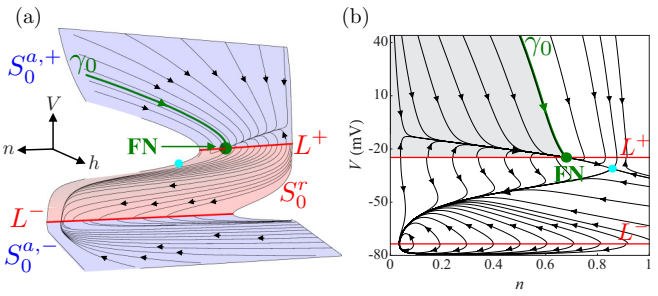

FIG. 3. Geometric structure of (1) for the parameter set in Table I. (a) The outer (blue) attracting sheets of S_0 are separated from the middle (red) repelling sheet by the (red) fold curves $L^{\pm}$. The slow flow (8) (black curves) is directed towards the folds. There is a folded node (FN, green) on L^+ with singular strong canard, γ_0 (green). The full system equilibrium (cyan) is a saddle. (b) Projection into the (V, n) plane. The funnel (gray) of the FN is enclosed by L^+ and γ_0.

by solutions of the two-dimensional (2D) *slow subsystem*

$$\begin{aligned} 0 &= f(v, n, h), \\ \frac{dn}{dt_s} &= g_1(v, n), \\ \frac{dh}{dt_s} &= g_2(v, h), \end{aligned} \tag{5}$$

obtained by taking the singular limit $\varepsilon \to 0$ in (2). The slow subsystem is the approximation of (2) in which the fast voltage variable moves so rapidly that it has already reached steady state and instantly adjusts to any changes in the gating variables. Recall that the idea of GSPT is to analyze the 1D fast and 2D slow subsystems, and combine their information in order to understand the origin and properties of the dynamics in the full three-dimensional (3D) system.

We begin with the 1D fast subsystem (4). The equilibria, S_0, of (4) form a cubic-shaped surface [in the (v, n, h) space] called the critical manifold

$$S_0 = \left\{ (v, n, h) : h_S = -\frac{\bar{g}_K n (v - \bar{V}_K)}{\bar{g}_{Ca} m_\infty(v)(v - \bar{V}_{Ca})} \right\}. \tag{6}$$

The outer sheets $S_0^{a,\pm}$ are stable and the middle sheet S_r is unstable; these are separated by curves $L^{\pm}$ of points corresponding to fold bifurcations of (4)

$$L^{\pm} = \left\{ (v, n, h) \in S_0 : \frac{\partial f}{\partial v} = 0 \right\}. \tag{7}$$

The conditions (7) reduce to lines on S_0 at constant voltage values (Fig. 3; red curves); L^+ and L^- denote the fold curves at depolarized and hyperpolarized voltages, respectively. Both also play the roles of firing thresholds. The V axis is also a fold curve (see Fig. 7 later).

From the linear stability analysis, we conclude that most solutions of (4) converge to the depolarized attracting sheet $S_0^{a,+}$ or the hyperpolarized attracting sheet $S_0^{a,-}$. Once trajectories reach one of these sheets, the dynamics slow down and the slow subsystem (5) becomes the appropriate approximating system. The algebraic equation in (5) constrains the phase space to the critical manifold, whilst the differential equations describe the slow motions along S_0. Thus, slow-fast analysis partitions the phase space into the fast dynamics away from S_0 together with the slow dynamics on S_0; S_0 is the interface where the fast and slow subsystems interact.

For the slow evolution on S_0, we have differential equations to describe the motions of n and h, while the algebraic equation implicitly describes the motions in v (slaved to S_0; Fig. 3 black curves). To obtain an explicit description of the v motions, we differentiate $f(v, n, h) = 0$ with respect to t_s, and use the graph representation (6) of the critical manifold. This gives

$$\begin{aligned} \frac{dv}{dt_s} &= -\left(\frac{\partial f}{\partial n} g_1 + \frac{\partial f}{\partial h} g_2 \right) \Big/ \frac{\partial f}{\partial v}, \\ \frac{dn}{dt_s} &= g_1, \end{aligned} \tag{8}$$

where h has been replaced by h_S. We stress that (8) is equivalent to (5); we simply incorporated the restriction to S_0 explicitly by setting $h = h_S$. In this formulation, we see that along the fold curves $L^{\pm}$ (where $\frac{\partial f}{\partial v} = 0$), the v equation of (8) has a singularity. Solutions of (8) that encounter $L^{\pm}$ blow-up in finite time and transition to the fast dynamics [34,35].

To aid our analysis of (8), which features this finite-time blow-up of solutions along $L^{\pm}$, we introduce an auxiliary time variable via $dt_s = -\frac{\partial f}{\partial v} dt_d$. This transforms the slow subsystem (8) to the *desingularized system*

$$\begin{aligned} \frac{dv}{dt_d} &= \frac{\partial f}{\partial n} g_1 + \frac{\partial f}{\partial h} g_2, \\ \frac{dn}{dt_d} &= -\left(\frac{\partial f}{\partial v} \right) g_1. \end{aligned} \tag{9}$$

In this setting, the singular points of (8) along $L^{\pm}$ were transformed into nullclines of (9). Since the transformation that led to (8) depends on (v, n, h), i.e., the transformation changes depending on where trajectories are in phase space, some care must be taken when comparing trajectories of the desingularized system (9) with those of the true slow subsystem (8). On the attracting sheets, $S_0^{a,\pm}$, the flow of (9) is topologically equivalent to the flow of (8) since $\frac{\partial f}{\partial v} < 0$ (and hence t_s and t_d have the same sign). On the repelling sheet, S_0^r, the flow of (9) is in the opposite direction to the flow of (8) since $\frac{\partial f}{\partial v} > 0$ (and hence t_s and t_d have opposite signs). With this relation between the slow and desingularized systems in mind, we analyze the dynamics of the desingularized system (9) to learn about the dynamics of the slow subsystem (8).

The desingularized system possesses two types singularities. Ordinary singularities are isolated points such that $\{g_1 = g_2 = 0\}$, and correspond to equilibria of the desingularized system (9), of the slow subsystem (8), and of the original model (1). For the parameter set in Table I, there is an ordinary singularity on S_0^r (Fig. 3; cyan), corresponding to a saddle equilibrium.

Folded singularities, M, are isolated points on $L^{\pm}$ where the right-hand side of the v equation in (9) is zero,

$$M = \left\{ (v, n, h) \in L^{\pm} : \frac{\partial f}{\partial n} g_1 + \frac{\partial f}{\partial h} g_2 = 0 \right\}. \tag{10}$$

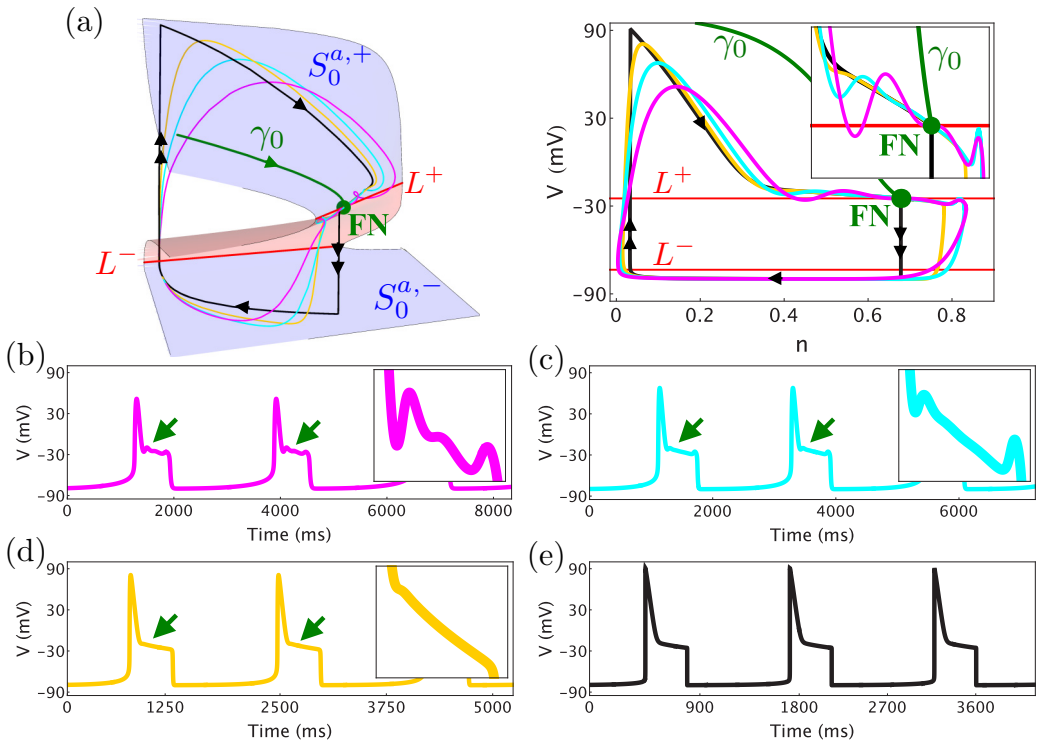

FIG. 4. Origin of EADs near the folded node (FN, green) for the standard parameters. (a) Left: singular (black) and nonsingular (magenta, cyan, and yellow) 1^3 attractor compared to S_0. All orbits enter $S_0^{a,+}$ inside the funnel between the singular strong canard γ_0 (green) and L^+ (red). Right: (V, n) projection. Inset: Zoom on FN. Corresponding voltage series are shown for (b) $C_m = 0.5\,\mu\text{F/cm}^2$ (magenta), (c) $C_m = 0.25\,\mu\text{F/cm}^2$ (cyan), (d) $C_m = 0.1\,\mu\text{F/cm}^2$ (yellow), and (e) $C_m = 0\,\mu\text{F/cm}^2$ (black).

Folded singularities are equilibria of the desingularized system (9), but not the slow subsystem (8) or the original model (1). Instead, they are points where both the numerator and denominator of the right-hand side of the v equation in (8) vanish at the same time, allowing for a cancellation of a simple zero. This means solutions of the slow subsystem may cross the folds (via a folded singularity) with finite speed and move from an attracting sheet to the repelling sheet (or vice versa). Such solutions are called *singular canards* [47], and play important roles in applications. We refer to [29,34,35] for extensive overviews of applications of folded singularities and canards in chemical, neural, and engineering contexts.

Folded singularities are classified as equilibria of the desingularized system. A folded singularity with real eigenvalues of the same sign is a folded node; real eigenvalues of opposite signs is a folded saddle; and complex conjugate eigenvalues is a folded focus. Folded nodes and folded saddles possess singular canards, whereas folded foci do not. The model cell has a folded node on L^+ for the standard parameter set (Fig. 3; green).

3. *EADs originate from a folded node*

We now demonstrate the origin of EADs in terms of the underlying geometric structures. To motivate this, we first take a 1^3 attractor of (1) (without stimulation) and compare it to S_0 in the (V, n, h) phase space [Fig. 4(a); magenta]. The three EADs can be seen as small loops in the magenta orbit about L^+. In the remaining panels we reduce C_m, or ε, to bring the system progressively closer to the singular limit described in Fig. 3. We observe that (i) the EADs are localized to the neighborhood of the folded node; (ii) by decreasing ε, the EADs decrease in amplitude (compare curves of different colors in Fig. 4); (iii) by decreasing ε, the location in phase space where the trajectory transitions from a depolarized state to a hyperpolarized state converges to the folded node. These observations lead us to hypothesize that the EADs observed for $0 < \varepsilon \ll 1$ arise from the folded node itself.

How do the small oscillations emerge from the folded node? To answer this, we examine how the sheets, $S_0^{a,+}$ and S_0^r, of the critical manifold persist for small and nonzero ε. As ε is increased away from zero, the attracting and repelling sheets, $S_0^{a,+}$ and S_0^r, perturb to attracting and repelling slow manifolds, $S_\varepsilon^{a,+}$ and S_ε^r, respectively [43,44]. These slow manifolds are the surfaces to which the slow segments of trajectories of (1) are slaved. Both $S_\varepsilon^{a,+}$ and S_ε^r are small and regular perturbations of $S_0^{a,+}$ and S_0^r, except in the neighborhood of the folded node, where they instead twist around a common axis of rotation [36,47]. The axis of rotation corresponds to the weak eigendirection of the folded node. The twisted slow manifolds are shown in Fig. 5 for various perturbations, corresponding to the C_m values used in Fig. 4. (For the purposes of visualization, the slow manifolds have only been computed up to a plane, Σ, passing through the folded node. The method of computation is detailed in [40].) The twisting of the slow manifolds (and the slow flow on them) is confined to an $\mathcal{O}(\sqrt{\varepsilon})$ neighborhood of the folded node [48]. Thus, the

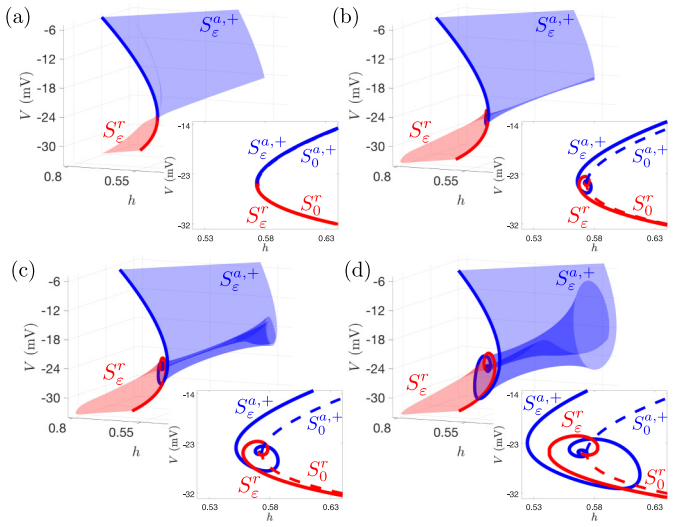

FIG. 5. Attracting (blue) and repelling (red) slow manifolds, $S_\varepsilon^{a,+}$ and S_ε^r, for (a) $C_m = 0.01\,\mu\text{F/cm}^2$, (b) $C_m = 0.1\,\mu\text{F/cm}^2$, (c) $C_m = 0.25\,\mu\text{F/cm}^2$, and (d) $C_m = 0.5\,\mu\text{F/cm}^2$. The twisting of the slow manifolds produces the EADs. Insets: Intersections of $S_\varepsilon^{a,+}$ (solid blue) and S_ε^r (solid red) with Σ. Also shown are the intersections of $S_0^{a,+}$ (dashed blue) and S_0^r (dashed red) with Σ. The folded node is at the intersection of the dashed blue and dashed red curves.

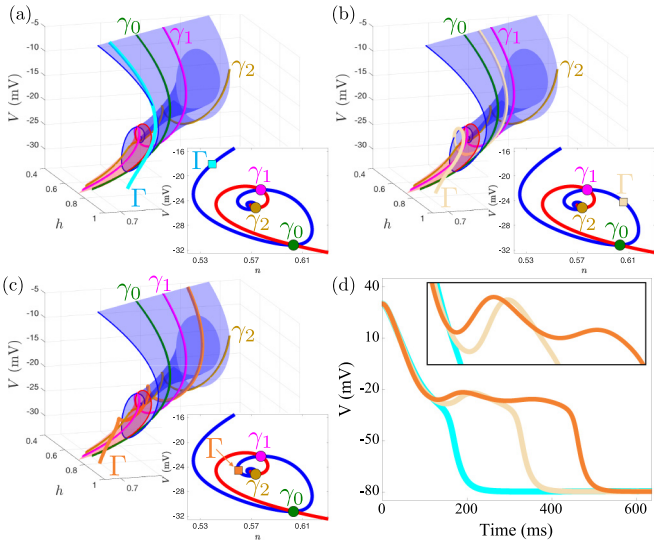

FIG. 6. Organization of EADs by maximal canards for the parameters in Table I. Only the first three maximal canards, γ_0 (green), γ_1 (magenta), and γ_2 (olive), are shown. (a) A solution (Γ; cyan) outside the rotational sectors has no EADs. (b) A solution (Γ; beige) in the sector between γ_0 and γ_1 has 1 EAD. (c) A solution (Γ; orange) in the sector between γ_1 and γ_2 has 2 EADs. (d) Time series, showing a regular AP (cyan), AP with 1 EAD (beige), and AP with 2 EADs (orange).

EADs arise from locally twisted slow manifolds around the folded node.

4. Canards organize the EADs

The local twisting of the slow manifolds results in a finite number of intersections between $S_\varepsilon^{a,+}$ and S_ε^r, called *maximal canards*. For the standard parameter set, there are five maximal canards. The outermost, γ_0, is the *maximal strong canard* and is the phase-space boundary between orbits that exhibit EADs near the folded node and orbits that do not (Fig. 6). That is, a solution of (1) with initial condition to the left of γ_0 in Fig. 6 is a regular 1^0 AP [Figs. 6(a) and 6(d); cyan curves]. A solution with initial condition between γ_0 and the maximal canard γ_1 executes 1 EAD near the folded node [Figs. 6(b) and 6(d); beige curves]. Any solution with initial condition enclosed by the canards γ_1 and γ_2 exhibits two EADs around the folded node [Figs. 6(c) and 6(d); brown curves]. In general, an orbit in the sector between the maximal canards γ_{k-1} and γ_k will execute k EADs. The innermost maximal canard, γ_w, is called the *maximal weak canard* and is the axis of rotation for both the slow manifolds and the other maximal canards [36,47]. Thus, the maximal canards partition the slow manifolds into sectors based on the rotational properties of solutions. In this way, the maximal canards organize the EADs in phase space; the path taken by the trajectory relative to the maximal canards determines the number of EADs produced.

5. Folded node and EAD dynamics are robust

Given that EADs arise from canard dynamics due to twisted slow manifolds around a folded node, is it possible to predict the number of maximal canards and associated EADs? The answer is "yes," and it is encoded in the strong and weak eigenvalues, $\lambda_s < \lambda_w < 0$, of the folded node (considered as an equilibrium of the desingularized system). Let $\mu = \frac{\lambda_w}{\lambda_s}$ denote the eigenvalue ratio. Then, provided ε is sufficiently small and $\mu \gg \sqrt{\varepsilon}$, the maximal number, $s_{\max}$, of EADs around the folded node is

$$s_{\max} = \left\lfloor \frac{\mu+1}{2\mu} \right\rfloor, \tag{11}$$

where $\lfloor \frac{\mu+1}{2\mu} \rfloor$ denotes the greatest integer less than or equal to $\frac{\mu+1}{2\mu}$ [47,48]. The corresponding number of maximal canards is $s_{\max}+1$. For the folded node in Figs. 3 to 6, $\mu \approx 0.13$ so that the maximal number of EADs possible is $s_{\max} = 4$, and there are five maximal canards.

Not only does the formula (11) predict the number of EADs, it also predicts how the number of EADs changes with parameters. Bifurcations of maximal canards occur whenever μ^{-1} passes through an odd integer value [36]. That is, if the system parameters are varied so that μ^{-1} increases through 3, then $s_{\max}$ increases from 1 to 2. If the system parameters are varied so that μ^{-1} increases through 5, then $s_{\max}$ increases from 2 to 3, and so on.

There are two special cases, $\mu = 0$ and $\mu = 1$, where the folded node ceases to exist and hence the canard-induced EADs are eliminated. The resonance $\mu = 1$ corresponds to the boundary where the folded node becomes a folded focus. Folded foci do not possess any canards. Hence, the $\mu = 1$ resonance serves as the transition between regular 1^0 APs and APs with EADs. This is illustrated in a two-parameter diagram, where the conductances of the K^+ current (g_K) and the K^+ Nernst potential (V_K) are varied and the asymptotic state of the system (1) is shown (Fig. 7). For parameter values within the region enclosed by the red $\mu = 1$ curve the folded

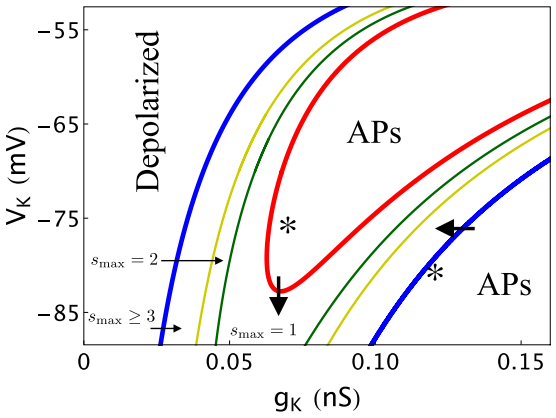

FIG. 7. Genericity of canard-induced EADs. The (g_K, V_K) plane has been partitioned according to the properties of the folded singularity. Folded nodes and EADs exist in the region enclosed by the outer $\mu = 0$ (blue) curves and the inner $\mu = 1$ (red) curve. Within this region, the maximal number of EADs that can be observed increases as the parameters are moved from the red $\mu = 1$ boundary to the blue $\mu = 0$ boundaries. The thick arrows indicate possible effects of drugs that reduce K^+ current conductance (leftward arrow) or increase the magnitude of the K^+ Nernst potential (downward arrow). The asterisks correspond to the (g_K, V_K) values used in Fig. 8.

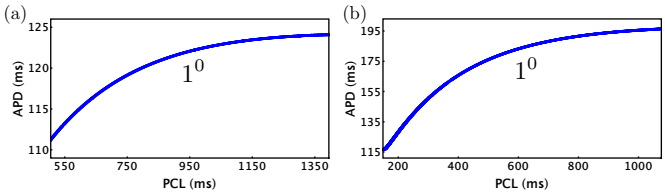

FIG. 8. The restitution curve is smooth when EADs are eliminated by (a) increasing the maximal conductance of K^+ channels ($g_K = 0.12\,\mathrm{mS/cm^2}$), or (b) decreasing the magnitude of the Nernst potential of K^+ channels ($g_K = 0.07\,\mathrm{mS/cm^2}$ and $V_K = -75$ mV). The APD versus PCL diagrams show a single branch corresponding to 1^0 APs [cf. Fig. 2(e)].

singularity is a folded focus, so only APs (without EADs) are produced.

The dark green curves in Fig. 7 are parameter combinations such that $\mu = 1/3$, so in the region delimited by these curves and the red $\mu = 1$ curve, $s_{max} = 1$ and APs with a single EAD are possible. On the olive curves $\mu = 1/5$ and in the region delimited by these curves and the dark green curves APs with two EADs are possible. This process can be continued to higher odd integer values of μ^{-1}; in the region between the olive curves and blue curves APs with three or more EADs are possible.

The $\mu = 0$ resonance (blue curves) is known as a folded saddle-node (FSN) bifurcation and can occur in several ways. The FSN bifurcation of type II (FSN II) is a bifurcation of the desingularized system in which a folded singularity and an ordinary singularity coalesce and swap stability in a hybrid transcritical bifurcation [49,50]. That is, for $\mu > 0$, the folded singularity on L^+ is a folded node and the ordinary singularity on S_0^r is a saddle. For $\mu < 0$, the folded singularity on L^+ is a folded saddle and the ordinary singularity has moved to $S_0^{a,+}$ where it is a stable node. Hence, the FSN II bifurcation corresponds to the transition between EADs and stable depolarized steady states (Fig. 7; left blue curve).

Another way in which a FSN bifurcation can occur is via a true transcritical bifurcation of folded singularities. That is, for $\mu > 0$, there is a folded node on L^+ and a folded saddle on the V axis. At $\mu = 0$, the folded node and folded saddle coalesce, and for $\mu < 0$, the folded singularity on L^+ is a folded saddle whereas the folded singularity on the V axis is a folded node. The slow flow around the folded node on the V axis is directed away from the V axis, and so EADs will not be observed. Thus, for $\mu < 0$, orbits of the slow flow encounter regular fold points on L^+, and the corresponding rhythm exhibits regular APs (without EADs). Hence, this FSN bifurcation corresponds to the transition between EADs and regular APs (Fig. 7; right blue curve).

The two-parameter diagram (Fig. 7) illustrates that, in this model, there is a large set of g_K, V_K parameters in which EADs can be produced. Thus, the behavior is generic, not limited to small regions of parameter space. It also illustrates the precision that GSPT provides in the determination of when EADs are possible, and the maximum number of EADs that are possible. Finally, it shows that decreasing the K^+ conductance, as is done with drugs like azimilide that act as K^+ channel antagonists, can induce EADs (thick leftward arrow). Also, increasing the magnitude of the K^+ Nernst potential, as in hypokalemia, can induce EADs (thick downward arrow). These observations are consistent with experimental studies [1,2,5]. Another prediction is that some manipulations can have biphasic responses. For example, reduction of K^+ conductance can take the model cell from a region of AP generation to a region of APs with EADS, but further reduction of the conductance can restore regular APs (inside the red curve in Fig. 7). To our knowledge, a systematic reduction of K^+ conductance using a tool such as the Dynamic Clamp has not been performed, as would be needed to test this prediction.

Figure 2(e) showed that when the model cell produces EADs the restitution curve (response of AP duration to changes in PCL) is complex. The restitution curve becomes much simpler when there are no EADs. Figure 8(a) shows that when g_K is increased so that the system lies within the right AP region of Fig. 7 (right asterisk) the AP duration increases smoothly with PCL. Similarly, when V_K is reduced in magnitude so that the system lies in the upper AP region of Fig. 7 (left asterisk), the AP duration increases smoothly with PCL [Fig. 8(b)]. Hence, the complex response of the model cell to changes in PCL is due to EADs, and a manipulation that eliminates EADs results in a much more regular behavior.

C. Periodic stimulation and mixed-mode oscillations

We established that EADs originate from canard dynamics around a folded node, and that the canards organize the EADs in both phase and parameter space. We now restore the periodic stimulation and study the stimulus-driven EAD attractors. Our aim is to explain the bifurcation diagram in

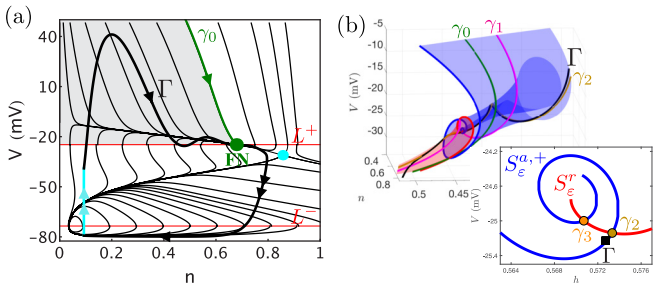

FIG. 9. Geometric mechanism for the stimulus-driven 1^2 attractor Γ (thick black and cyan). Parameters are set at those in Fig. 2(a) with PCL = 1200 ms. (a) Comparison of Γ to the slow flow (thin black) and geometric structures. The stimulus (cyan segment) induces a transition from the hyperpolarized sheet to the funnel (shaded) of FN. (b) Comparison of Γ to the slow manifolds; Γ lies in the sector between γ_1 and γ_2, and thus has two EADs.

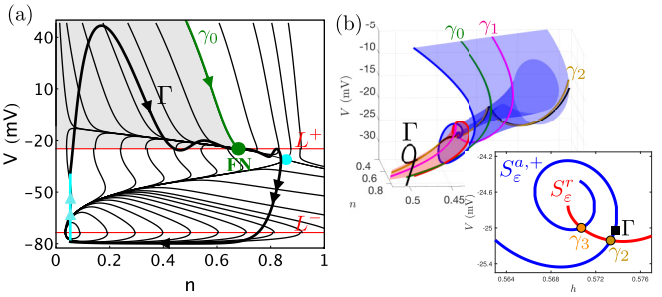

FIG. 10. Local and global mechanisms for a stimulus-driven 1^3 attractor Γ (thick black and cyan). Parameters are as in Fig. 2(d) with PCL = 1500 ms. (a) Comparison of Γ to the slow flow (thin black) and geometric structures in the (V, n) projection. (b) The orbit is injected into the sector delimited by the canards γ_2 and γ_3, and hence exhibits three EADs.

Fig. 2. We will show that the variety of AP morphologies exhibited under various PCLs can be explained by the canards.

1. High- and low-frequency pacing: Canard-induced mixed-mode oscillations

Recall that when there is periodic stimulation I_{sti}, the system entrains to the driving oscillator. For low PCLs (i.e., high-frequency pacing), the attractor is a 1^2 AP with EADs [Figs. 2(a) and 2(e)]. Using the results of our geometric analysis, we deconstruct the 1^2 rhythm (Fig. 9) and find that it consists of the following:

(i) canard-induced EADs around the folded node due to twisted slow manifolds;

(ii) a fast transition from the depolarized folded node region to the hyperpolarized slow manifold; and

(iii) a stimulus-driven transition from the hyperpolarized slow manifold to the depolarized slow manifold.

Note in Fig. 9(a) that the weak canard is approximately given by the stable manifold of the (cyan) saddle, and that the EADs are centered on this weak canard (i.e., the weak canard is the axis of rotation).

The periodic stimulus provides the mechanism for returning orbits to the neighborhood of the folded node. More specifically, the stimulus switches "on" during the slow hyperpolarized segment of the trajectory. This drives the orbit away from the hyperpolarized sheet and into the basin of attraction of the depolarized sheet $S_\varepsilon^{a,+}$. The timing of the stimulus is such that the orbit is injected into the rotational sector enclosed by the maximal canards γ_1 and γ_2, and hence exhibits two EADs. This combination of a local canard mechanism (for the EADs) and a global (stimulus-induced) return mechanism is known as a canard-induced mixed-mode oscillation (MMO) [48].

Similarly, for large PCLs (i.e., low-frequency pacing), the stimulus-driven 1^3 attractor is a canard-induced MMO with period set by the PCL [Figs. 2(d) and 2(e)]. The 1^3 MMO attractor consists of (local) canard-induced EADs around the folded node combined with a global stimulus-driven return that projects orbits from the hyperpolarized sheet into the rotational sector enclosed by the canards γ_2 and γ_3 (Fig. 10).

2. Intermediate-frequency pacing: EAD alternans due to reinjection into adjacent rotational sectors

In Fig. 2(e), we found a band of intermediate pacing frequencies for which the stimulus-driven attractor is a $1^2 1^3$ alternator [e.g., Fig. 2(b)]. We compare the $1^2 1^3$ attractor to the underlying geometric structures in Fig. 11. As in the low- and high-frequency forcing cases, the 1^2 and 1^3 segments are each canard-induced MMOs. The difference here is that the timing of the stimulus is such that the orbit visits different (contiguous) rotational sectors on each stimulus pulse.

The $1^2 1^3$ alternans attractor $\Gamma = \Gamma_2 \Gamma_3$ decomposes as follows. Starting on the hyperpolarized sheet, the first stimulus pulse [Fig. 11(a); leftmost cyan segment] projects the orbit into the sector enclosed by γ_2 and γ_3, so it exhibits three EADs [Fig. 11(b); Γ_3]. The orbit then transitions to the hyperpolarized sheet where it drifts towards the firing threshold L^-. Before it can reach L^-, the next stimulus pulse [Fig. 11(a); rightmost cyan segment] projects the orbit into the sector enclosed by γ_1 and γ_2 [Fig. 11(b); Γ_2], and thus Γ exhibits two EADs. The orbit then returns to the hyperpolarized sheet where it again slowly drifts towards L^-. Since Γ_2 only has two EADs, the APD is shorter (compared to Γ_3) and the corresponding diastolic interval (DI) is longer. As such, the

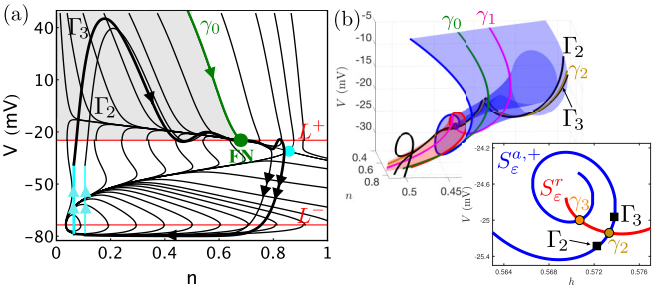

FIG. 11. Geometric mechanism for stimulus-driven $1^2 1^3$ alternans, $\Gamma = \Gamma_2 \Gamma_3$. Parameters are as in Fig. 2(b) with PCL = 1300 ms. (a) Comparison of Γ to the slow flow (thin black). The stimulus (cyan) projects Γ into the funnel at different locations, causing Γ to visit different rotational sectors. (b) Γ alternately enters the sector between γ_1 and γ_2 (two EADs), and the sector between γ_2 and γ_3 (three EADs).

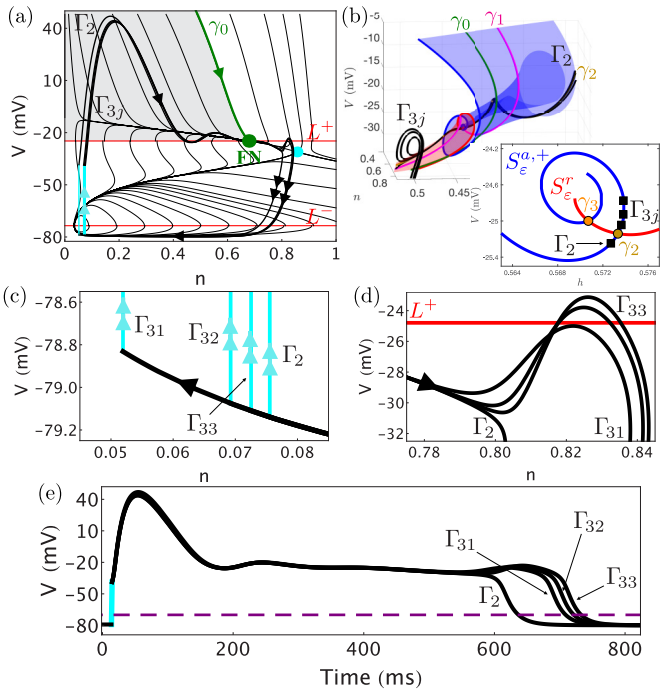

FIG. 12. Sensitivity of the EADs near a maximal canard. The cause for the variability in the number and magnitude of the EADs is that Γ peels off γ_2 at different times. Parameters are as in Fig. 2(c) with PCL = 1200 ms. (a) Projection of the $1^2(1^3)^3$ attractor, Γ, into the (V, n) plane. (b) The orbit stays close to the maximal canard γ_2 on each return to $S_\varepsilon^{a,+}$. (c) Zoom of the (V, n) plane where the stimuli are applied. (d) Zoom of the EADs as they peel off γ_2. (e) Time series of Γ_2 and Γ_{3j} for $j = 1, 2, 3$. The APD (DI) is the time spent above (below) the (dashed purple) threshold $V = -70$ mV.

orbit is able to drift further along the hyperpolarized sheet before the next stimulus occurs. Once the stimulus "switches on," the process repeats periodically, thus producing the $1^2 1^3$ attractor. Hence, at this intermediate stimulus frequency there is an alternation between two different points on the hyperpolarized sheet at which the stimulus is applied, and from these positions the orbits enter adjacent rotational sectors on the depolarized sheet, resulting in two alternating EAD profiles.

3. Intermediate-frequency pacing: Dynamical chaos and intermittency due to sensitivity near maximal canards

In Fig. 2(e), we found a band of pacing frequencies for which the model exhibited seemingly chaotic and intermittent behavior. We show, for a representative $1^2(1^3)^3$ attractor Γ, that the complex signatures arise from the crossing of a maximal canard (Fig. 12). As before, each AP with EADs is a canard-induced MMO. The variability in the number and magnitude of the EADs is due to the stimulus, which perturbs the orbit from the hyperpolarized sheet at different locations on each pulse.

Let Γ_2 denote the 1^2 segment of Γ, and Γ_{3j}, $j = 1, 2, 3$ denote the 1^3 segments of Γ, i.e., $\Gamma = \Gamma_2 \cup \Gamma_{31} \cup \Gamma_{32} \cup \Gamma_{33}$. Starting with Γ_2, the stimulus [Fig. 12(c); cyan] induces a fast transition to the depolarized sheet close to γ_2 in the sector between γ_1 and γ_2 [Fig. 12(b)], and hence there are two EADs. The intrinsic dynamics of the model cell return Γ_2 to $S_\varepsilon^{a,-}$ where it drifts to smaller n. The next stimulus initiates Γ_{31} and projects the orbit into the sector bound by γ_2 and γ_3. The additional EAD in Γ_{31} extends the APD compared to that of Γ_2 [Fig. 12(e)]. As such, the DI of Γ_{31} is shorter than that of Γ_2. This means Γ_{32} is initiated on $S_\varepsilon^{a,-}$ at a larger n value [Fig. 12(c)], and enters $S_\varepsilon^{a,+}$ closer to γ_2. Since Γ_{32} follows γ_2 more closely than Γ_{31}, the (i) EADs are larger amplitude [Fig. 12(d)], (ii) APD is longer, and (iii) DI is shorter. Consequently, Γ_{33} is initiated on $S_\varepsilon^{a,-}$ at a larger n value, enters $S_\varepsilon^{a,+}$ closer to γ_2, and hence exhibits the (i) largest EADs, (ii) longest APD, and (iii) shortest DI.

The other complex MMO signatures in Fig. 2(e) emerge by the same mechanism. That is, the $(1^2)^p(1^3)^q$ attractors for $p, q \in \mathbb{N}$ arise because the PCL is such that the orbit enters the depolarized sheet close to the maximal canard γ_2. Since the behavior of trajectories near a maximal canard is exponentially sensitive [36], small changes in PCL manifest as significant changes in the number, amplitude, and duration of EADs on each pulse. Likewise, at such PCL values, small changes in initial conditions have large effects on the V time course, the hallmark of chaos.

IV. DISCUSSION

It has been previously demonstrated that early afterdepolarizations produced by a simple cardiomyocyte model [2], a reduction of the Luo-Rudy 1 (LR1) model [37], are the consequence of carnard dynamics in the vicinity of a folded node [31], a result further illuminated through the geometric analysis shown in Figs. 3 to 6. We show that these dynamics are robust in (g_K, V_K) (Fig. 7). These parameters are chosen since they can be modulated by drugs or environment; g_K is reduced by K^+ channel antagonists such as azimilide, while V_K is increased in magnitude in hypokalemia. Figure 7 predicts that both manipulations can induce EADs, and indeed both manipulations have been shown to do this in experiments [1,2,5].

Our second set of results involves the paced system, which receives periodic depolarizing stimuli (Fig. 2). Each pulse pushes an orbit into the basin of attraction of the depolarized sheet, triggering an action potential that can be a mixed-mode oscillation if EADs are produced. For high- and low-frequency pacing, orbits land in the rotational sectors delimited by maximal canards and stay far from the maximal canards, so that the voltage time course exhibits regular, periodic behavior. At high stimulus frequencies, the orbits land in the sector between γ_1 and γ_2, so each AP has two EADs. At low stimulus frequencies, the orbits land in the sector between γ_2 and γ_3, so each AP has three EADs. The number of EADs depends on the rotational sector in which the orbit lands in response to the stimulus (Figs. 9 to 12). The EAD alternans observed for intermediate frequencies emerge because the stimulus alternately projects the orbit into different sectors on each pulse. In some cases, the outcome can be complex, with a sequence of MMOs of different durations and numbers of EADs. This behavior was referred to as "dynamical chaos" in earlier publications [2,23].

The LR1 (and reduced LR1) model is a three timescale system with fast voltage dynamics, intermediate activa-

tion dynamics for the K^+ channels, and slow inactivation dynamics for the L-type Ca^{2+} channels. Prior slow-fast analyses [2,23,27,30] were performed treating V and n as fast, and h as slow. EADs were shown to arise from delayed Hopf bifurcations [51]. While this 1-slow-2-fast approach explains certain aspects of EADs, it cannot predict the number (i.e., duration) of EADs nor explain why EADs change with PCL. The 2-slow-1-fast approach taken here fills these gaps. It explains the origin of the EADs in terms of twisted slow manifolds and folded node canards, and explains how the AP morphologies change with parameters and PCLs. To reconcile the complementary and nonoverlapping results from the 2-fast-1-slow and 1-fast-2-slow approaches, a three timescale analysis needs to be done. Such analyses were performed in three timescale models of pituitary lactotrophs [52,53]. We conjecture that the delayed Hopf bifurcation of the 1-slow-2-fast approach and the folded node of the 2-slow-1-fast approach are different unfoldings of a more degenerate singularity that can only be revealed by three timescale analysis. We leave this to future work.

The advantage of the minimal model for the analysis presented here is its low dimensionality. More realistic cardiomyocyte models can have 40 or more dimensions, reflecting many types of ionic currents and in many cases equations for Ca^{2+} handling in the cytosol, the sarcoplasmic reticulum (SR), and the subspace between the SR and the cell membrane [22,54–57]. One major advantage of these larger models is that they have more biological detail that allows for simulation of, for example, the application of pharmacological agents that act as antagonists for specific types of ion channels, such as inward-rectifying K^+ channels, while the minimal model incorporates only a single type of K^+ current and a single type of Ca^{2+} current. With the correct parametrizations, these more complete models are capable of reproducing the various forms of EADs that were characterized, each with different, but partially overlapping, biophysical mechanisms [58], while the minimal model was developed to produce EADs of a particular type. EADs are divided broadly into types according to the timing of the events: "phase-2 EADs" occur during the plateau of an elongated AP, and "phase-3 EADs" occur during the falling phase of the AP. There are also "depolarizing afterdepolarizations" that occur after the completion of the AP. Our analysis on a minimal model suggests that the dynamics underlying some phase-2 EADs are canard-induced, and we speculate this will be the case in more complete biophysical models. While the full slow or fast analysis done with the minimal model is not possible with the high-dimensional models, it is possible to perform a less complete analysis, such as determining the existence of folded node singularities. Indeed, such an analysis is important for establishing that canard dynamics are the basis of phase-2 EADs in more complete models, and is currently being undertaken by our group.

Why does it matter whether EADs are due to canard dynamics near a folded node singularity? Although it sounds abstract, the ramifications of knowing this can be important and useful. As we demonstrate, if the EADs are associated with a folded node, then one can simply analyze the eigenvalues of the desingularized reduced system at the folded node to determine how many EADs are possible, at least when the system is near the singular limit as it is in this model. One can also determine parameter changes that enhance or eliminate EAD production. In particular, one can determine regions of parameter space where canard-induced EADs are not possible, without the need to perform any numerical integrations (as in Fig. 7 and [31]). So once EADs are linked to folded nodes, one gains a great deal of predictive capability. In addition to this, knowing the dynamical mechanism for the EADs helps in the understanding of complex behavior, such as dynamical chaos, that would be hard or impossible to understand from the viewpoint of interacting ionic currents (i.e., a biophysical interpretation). Knowing which ion channels are key players in EADs is of course important, and can provide targets for pharmacological or genetic manipulation, but the complexity of the multiscale nonlinear dynamical system provides limitations to interpreting behavior without mathematical tools such as GSPT.

The theory of folded singularities has been applied to numerous systems. This includes intracellular Ca^{2+} dynamics [59], the electrical activity of neurons [60–62] and pituitary cells [53], and MMOs that are likely canard-induced were observed in the oxidation of platinum [63], dusty plasmas [64], and chemical oscillations [65,66]. The demonstration that some forms of EADs are canard-induced in a minimal cardiomyocyte model adds cardiac cells to the growing list of the biological and chemical systems whose dynamics are organized by folded singularities. Our system is different, however, in that it is periodically forced under physiological conditions, where the forcing is initiated at the sinoatrial node. As we demonstrate here, this forcing can lead to complicated dynamics due to the injection of the orbit into different rotational sectors, so that the number of EADs produced following each stimulus can vary. The result can appear to be unpredictable, and chaotic, and sensitive to small changes in the forcing frequency and initial conditions. Whether this complex behavior is exhibited in a physiological setting, within an intact heart, is unclear. It is generally accepted that EADs can lead to arrythmias [9,16–18], including ventricular tachycardia, but it has not been established that complex, chaotic behavior at the single myocyte level contributes to this.

[1] R. V. Madhvani, Y. Xie, A. Pantazis, A. Garfinkel, Z. Qu, J. N. Weiss, and R. Olcese, J. Physiol. **589**, 6081 (2011).

[2] D. Sato, L. Hua Xie, T. P. Nguyen, J. N. Weiss, and Z. Qu, Biophys. J. **99**, 765 (2010).

[3] Y. Xie, F. Chen, H. S. Karagueuzian, and J. N. Weiss, Circ. Res. **104**, 79 (2008).

[4] D. Guo, X. Zhao, Y. Wu, T. Liu, P. R. Kowey, and G.-X. Yan, J. Cardiovasc. Electrophysiol. **18**, 196 (2007).

[5] G.-X. Yan, Y. Wu, T. Liu, J. Wang, R. A. Marinchak, and P. R. Kowey, Circulation **103**, 2851 (2001).

[6] S. Nobe, M. Aomine, and M. Arita, Gen. Pharmacol. **1993**, 1187 (1993).

[7] E. Winslow, J. K. Campbell, and R. J. Marshall, J. Cardiovasc. Pharmacol. **8**, 1208 (1986).

[8] S. G. Priori and P. B. Corr, Am. J. Physiol. **258**, H1796 (1990).

[9] W. Shimizu, T. Ohe, T. Kurita, H. Takaki, N. Aihara, S. Kamakura, M. Matsuhisa, and K. Shimomura, Circulation **84**, 1915 (1991).

[10] J. M. Davidenko, L. Cohen, R. Goodrow, and C. Antzelevitch, Circulation **79**, 674 (1989).

[11] C. T. January and J. M. Riddle, Circ. Res. **1989**, 977 (1989).

[12] Y. Asano, J. M. Davidenko, W. T. Baxter, R. A. Gray, and J. Jalife, J. Am. Coll. Cardiol. **29**, 831 (1997).

[13] N. El-Sherif and G. Turitto, Curr. Opin. Cardiol. **18**, 6 (2003).

[14] C. Napolitano, S. G. Priori, P. J. Schwartz, R. Bloise, E. Ronchetti, J. Nastoli, G. Bottelli, M. Cerrone, and S. Leonardi, J. Am. Med. Assoc. **294**, 2975 (2005).

[15] W. Shimizu, T. Ohe, T. Kurita, T. Tokuda, and K. Shimomura, J. Cardiovasc. Electrophysiol. **5**, 438 (1994).

[16] P. F. Cranefield and R. S. Aronson, Cardiovasc. Drugs Ther. **5**, 531 (1991).

[17] C. Lerma, T. Krogh-Madsen, M. Guevara, and L. Glass, J. Stat. Phys. **128**, 347 (2007).

[18] W. Shimizu and C. Antzelevitch, Circulation **96**, 2038 (1997).

[19] S. M. Pogwizd and D. M. Bers, Trends Cardiovas. Med. **14**, 61 (2004).

[20] M. C. Sanguinetti and M. Tristani-Firouzi, Nature **440**, 463 (2006).

[21] Y. Kurata, K. Tsumoto, K. Hayashi, I. Hisatome, M. Tanida, Y. Kuda, and T. Shibamoto, Am. J. Physiol. **312**, H106 (2017).

[22] C. H. Luo and Y. Rudy, Circ. Res. **74**, 1097 (1994).

[23] D. X. Tran, D. Sato, A. Yochelis, J. N. Weiss, A. Garfinkel, and Z. Qu, Phys. Rev. Lett. **102**, 258103 (2009).

[24] J. Zeng and Y. Rudy, Biophys. J. **68**, 949 (1995).

[25] E. de Lange, Y. Xie, and Z. Qu, Biophys. J. **103**, 365 (2012).

[26] R. Huffaker, S. T. Lamp, J. N. Weiss, and B. Kogan, Heart Rhythm **1**, 441 (2004).

[27] D. Sato, L. Hua Xie, A. A. Sovari, D. X. Tran, N. Morita, F. Xie, H. Karagueuzian, A. Garfinkel, J. N. Weiss, and Z. Qu, Proc. Nat. Acad. Sci. USA **106**, 2983 (2009).

[28] N. Vandersickel, I. V. Kazbanov, A. Nuitermans, L. D. Weise, R. Pandit, and A. V. Panfilov, PLoS One **9**, e84595 (2014).

[29] R. Bertram and J. Rubin, Math. Biosci. **287**, 105 (2017).

[30] P. Kügler, PLoS One **11**, e0151178 (2016).

[31] P. Kügler, A. H. Erhardt, and M. A. K. Bulelzai, PLoS One **13**, e0209498 (2018).

[32] T. Vo, R. Bertram, J. Tabak, and M. Wechselberger, J. Comput. Neurosci. **28**, 443 (2010).

[33] B. P. Damiano and M. R. Rosen, Circulation **69**, 1013 (1984).

[34] M. Desroches, J. Guckenheimer, B. Krauskopf, C. Kuehn, H. M. Osinga, and M. Wechselberger, SIAM Rev. **54**, 211 (2012).

[35] C. Kuehn, *Multiple Time Scale Dynamics*, Applied Mathematical Sciences Vol. 191 (Springer, New York, 2015).

[36] M. Wechselberger, SIAM J. Appl. Dyn. Syst. **4**, 101 (2005).

[37] C. H. Luo and Y. Rudy, Circ. Res. **68**, 1501 (1991).

[38] B. Ermentrout, XPP/XPPAUT Homepage (2016), http://www.math.pitt.edu/~bard/xpp/xpp.html.

[39] E. J. Doedel, B. E. Oldeman, A. R. Champneys, F. Dercole, T. Fairgrieve, Y. Kuznetsov, R. Paffenroth, B. Sandstede, X. Wang, and C. Zhang, AUTO: Software for Continuation and Bifurcation Problems in Ordinary Differential Equations (2011), http://indy.cs.concordia.ca/auto/.

[40] M. Desroches, B. Krauskopf, and H. M. Osinga, SIAM J. Appl. Dyn. Syst. **7**, 1131 (2008).

[41] M. Desroches, B. Krauskopf, and H. M. Osinga, Nonlinearity **23**, 739 (2010).

[42] M. L. Koller, M. L. Riccio, and J. R. F. Gilmour, Am. J. Physiol. **275**, H1635 (1998).

[43] N. Fenichel, J. Differential Equations **31**, 53 (1979).

[44] C. Jones, in *Dynamical Systems, Montecatini Terme*, Lecture Notes in Math. Vol. 1609, edited by L. Arnold (Springer, Berlin, 1994), pp. 44–118.

[45] J. Rinzel, A formal classification of bursting mechanisms in excitable systems, in *Mathematical Topics in Population Biology, Morphogenesis, and Neurosciences*, Lecture Notes in Biomathematics, edited by E. Teramoto and M. Yamaguti, (Springer, Berlin, 1987), pp. 267–281.

[46] Y. Xie, G. Hu, D. Sato, J. N. Weiss, A. Garfinkel, and Z. Qu, Phys. Rev. Lett. **99**, 118101 (2007).

[47] P. Szmolyan and M. Wechselberger, J. Differential Equations **177**, 419 (2001).

[48] M. Brøns, M. Krupa, and M. Wechselberger, in *Bifurcation Theory and Spatio-Temporal Pattern Formation*, Fields Institute Communications Vol. 49 (American Mathematical Society, Providence, RI, 2006), pp. 39–63.

[49] J. Guckenheimer, Chaos **18**, 015108 (2008).

[50] M. Krupa and M. Wechselberger, J. Differential Equations **248**, 2841 (2010).

[51] S. M. Baer, T. Erneux, and J. Rinzel, SIAM J. Appl. Math. **49**, 55 (1989).

[52] W. Teka, J. Tabak, and R. Bertram, Chaos **22**, 043117 (2012).

[53] T. Vo, R. Bertram, and M. Wechselberger, SIAM J. Appl. Dyn. Syst. **12**, 789 (2015).

[54] C. H. Luo and Y. Rudy, Circ. Res. **74**, 1071 (1994).

[55] Y. Kurata, I. Hisatome, H. Matsuda, and T. Shibamoto, Biophys. J. **89**, 2865 (2005).

[56] T. O'Hara, L. Virág, A. Varró, and Y. Rudy, PLoS Comput. Biol. **7**, e1002061 (2011).

[57] S. B. Williams, G. D. Smith, E. A. Sobie, and M. S. Jafri, Math. Biosci. **226**, 1 (2010).

[58] C. Antzelevitch and A. Burashnikov, Card. Electrophysiol. Clin. **3**, 23 (2011).

[59] E. Harvey, V. Kirk, M. Wechselberger, and J. Sneyd, J. Nonlinear Sci. **21**, 639 (2011).

[60] H. G. Rotstein, M. Wechselberger, and N. Kopell, SIAM J. Appl. Dyn. Syst. **7**, 1582 (2008).

[61] J. Rubin and M. Wechselberger, Biol. Cybernet. **97**, 5 (2007).

[62] J. Rubin and M. Wechselberger, Chaos **18**, 015105 (2008).

[63] M. Krischer, M. Eiswirth, and G. Ertl, J. Chem. Phys. **96**, 9161 (1992).

[64] M. Mikikian, M. Cavarroc, L. Couëdel, Y. Tessier, and L. Boufendi, Phys. Rev. Lett. 225005 **100** (2008).

[65] V. Petrov, S. K. Scott, and K. Showalter, J. Chem. Phys. **97**, 6191 (1992).

[66] H. G. Rotstein, N. Kopell, A. M. Zhabotinsky, and I. Epstein, J. Chem. Phys. **119**, 8824 (2003).